metals

MDPI

Article

Constitutive Equation of GH4169 Superalloy and Microstructure Evolution Simulation of Double-Open Multidirectional Forging

Yongbo Jin [1,2], Hao Xue [1], Zheyi Yang [1], Lili Zhang [3], Chunxiang Zhang [2], Sirui Wang [1] and Junting Luo [1,2,*]

1 Education Ministry Key Laboratory of Advanced Forging & Stamping Technology and Science, Yanshan University, Qinhuangdao 066004, China; ysu18203350795@163.com (Y.J.); 15667079639@163.com (H.X.); 18840871396@163.com (Z.Y.); xichenxu123@163.com (S.W.)

2 State Key Laboratory of Metastable Materials Science and Technology, Yanshan University, Qinhuangdao 066004, China; zhangchunxiang@ysu.edu.cn

3 School of Art and Design, Yanshan University, Qinhuangdao 066004, China; 18712761815@163.com

* Correspondence: luojunting@ysu.edu.cn; Tel.: +86-335-805-2253

Received: 4 September 2019; Accepted: 24 October 2019; Published: 25 October 2019

Abstract: This paper presented a double-open multidirectional forging with relatively few deformation passes and a uniform deformation. The constitutive equation and dynamic recrystallization model of the GH4169 superalloy were identified based on a thermal compression test and imported into Deform simulation software. The microstructure evolution law of GH4169 superalloy undergoing double-open multidirectional forging was simulated. The evolution of the recrystallization volume fraction and recrystallized grain size of the GH4169 superalloy during double-open multidirectional forging was obtained. Both higher temperatures and more passes were found to produce more complete recrystallization and smaller recrystallization grain size. At the maximum temperature studied, 1000 °C, with nine passes, the recrystallization volume fraction exceeded 95%, and the recrystallized grain size reached 3–5.5 μm.

Keywords: constitutive equation; GH4169 superalloy; microstructure evolution simulation; multidirectional forging

1. Introduction

GH4169 alloy is a nickel-based superalloy that is extensively used in a steam turbine, aerospace, chemical, and nuclear industries [1–3]. However, the original blanks produced during casting are unsatisfactory due to increased performance requirements, and thus, must be improved to meet the performance standards [4–6]. Multidirectional forging is a plastic processing method for obtaining a fine grain structure by continuously changing the direction of axial external loads, thereby compressing the forgings in different directions [7]. Multidirectional forging is a plastic processing method to obtain fine grain structure by continuously changing the direction of axes of external loads and compressing forgings in different directions. The multi-directional forging process can improve the microstructure of the material and obtain fine-grained microstructure materials with excellent mechanical properties and uniform properties. This process is particularly suitable for the regulation of the structure and properties of GH4169 alloy materials.

In recent years, research on the multidirectional forging process in the process of thermal deformation has gradually increased at home and abroad. Mikhail et al. [8] mainly studied the influence of isothermal multi-directional forging on the microstructure evolution of conventional Al-Mg-based alloys in the strain range of 1.5–6.0 and the temperature range of 200–500 °C. Xia et al. [9] conducted

a multi-directional forging of Mg-Gd-Y-Nd-Zr alloy at low temperatures to study grain refinement, microstructure, and uniformity of the mechanical properties. Aoba et al. [10] systematically studied the microstructure evolution and mechanical properties of 6000 series aluminum alloys subjected to multi-directional forging and artificial aging treatment. Lin et al. [11] derived a constitutive and microstructure evolution model for GH4169 superalloy based on equivalent dislocation density. However, relevant studies on the simulation of multi-directional forging microstructures are still rare.

In this study, a double-open multidirectional forging with relatively few deformation passes and uniform deformation was generated. The constitutive equation and dynamic recrystallization model were formulated based on a thermal compression experiment on the GH4169 superalloy. The model was then imported into the DEFORM simulation software. The design process of double-open multidirectional forging was explored, and specifically, the predictions of the recrystallization volume fraction and grain size as functions of temperature during the microstructure evolution simulation of GH4169 superalloy were discussed.

2. Experimental Materials and Methods

The material used in the experiment was a GH4169 alloy cylinder (φ 6 mm × 9 mm). The original microstructure of the sample was approximately uniform equiaxed, and the average grain size was approximately 25 μm, as shown in Figure 1. Heat treatment is necessary for the dynamic-recrystallization hot compression test of the samples. The equipment used in the experiment was the Gleeble-3800 Thermal Simulation Tester, and the specific process parameters are shown in Table 1. Figure 2 shows a flowchart of the GH4169 superalloy hot compression test. For the Gleeble-3800 thermal compression test, the alloy samples were initially heated at a rate of 5 °C/s to the required temperature (900 °C, 950 °C, 1000 °C, 1050 °C, or 1120 °C) for the experiment. Once the desired temperature was maintained for 2 min, the sample was subjected to a hot compression test at different strain rates (0.001, 0.01, 0.1, and 1 s^{-1}). Each sample was immediately water-cooled at the end of the experiment [12–14].

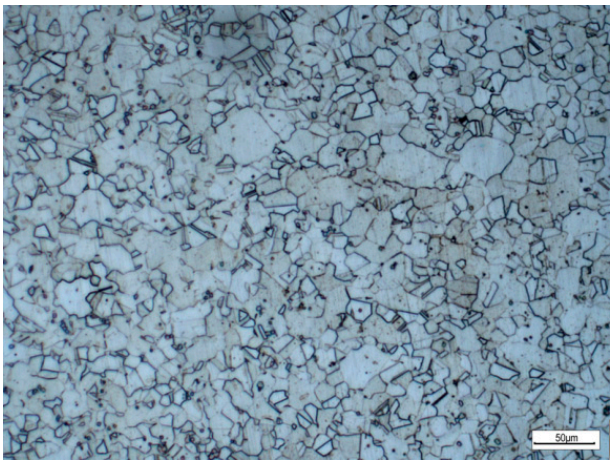

Figure 1. The original microstructure of the GH4169 forge piece.

Table 1. Deformation parameters for the GH4169 superalloy hot compression experiment.

Temperature/°C	900	950	1000	1050	1120
Strain rate/s^{-1}	0.001, 0.01, 0.1, 1				
Heating rate/°C·s^{-1}	5				
Compression ratio	0.6				

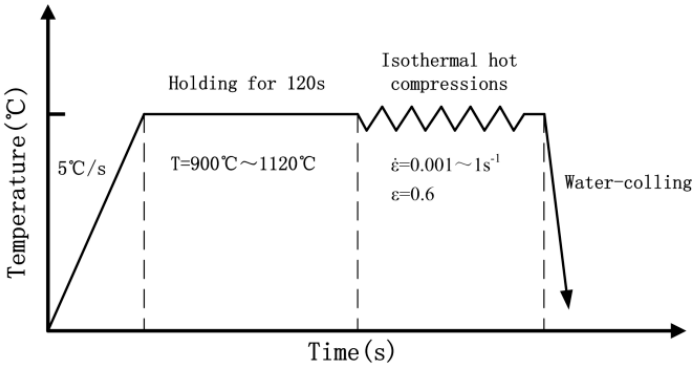

Figure 2. Flowchart of the GH4169 superalloy hot compression experiment.

3. Results and Discussion

3.1. True Stress-Strain Curve at Different Strain Rates

Figure 3 shows the true stress-strain curve obtained for the GH4169 superalloy at different strain rates and temperatures. The stress gradually decreased with an increase in temperature at a given strain and strain rate. Both the peak stress and strain point corresponding to the peak stress gradually decreased with increasing temperature. The material had a similar response to thermal deformation at different strain rates; that is, the stress value increased with the deformation amount. Meanwhile, the stress value decreased with an increase in deformation when the stress value reached its maximum (peak stress). Furthermore, the stress of the material remained constant with the increase in strain when the stress value reached steady-state stress.

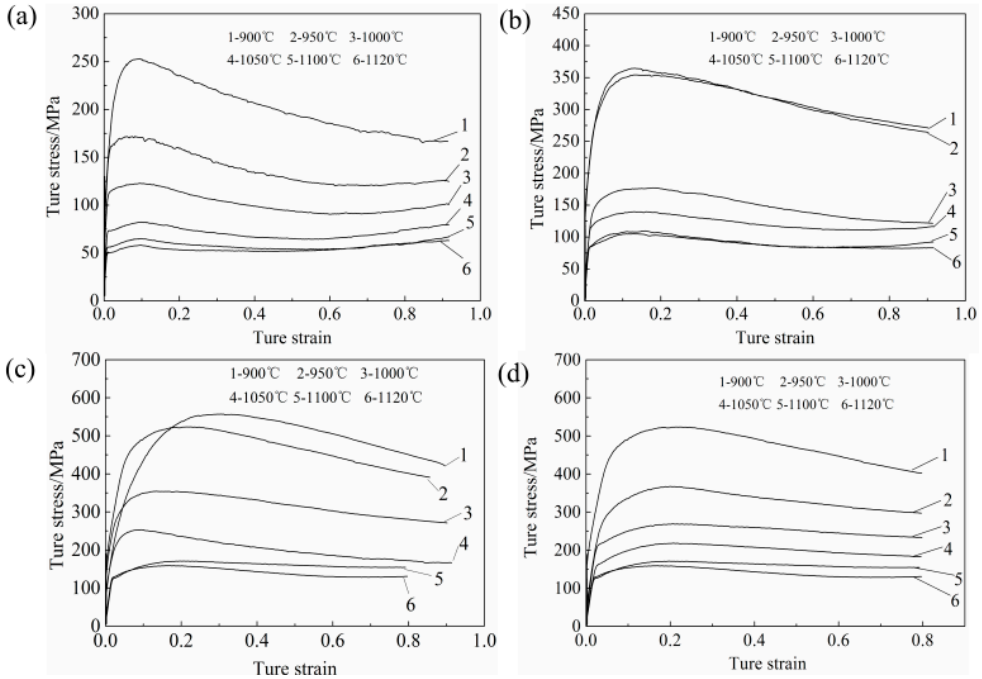

Figure 3. Thermal compression strain curve of GH4169 alloy under different strain rates and temperatures. (**a**) $\dot{\varepsilon} = 0.001s^{-1}$; (**b**) $\dot{\varepsilon} = 0.01s^{-1}$; (**c**) $\dot{\varepsilon} = 0.1s^{-1}$; (**d**) $\dot{\varepsilon} = 1s^{-1}$.

The sharp increase of stress in the initial stage of thermal compression deformation was due to work hardening. Although recovery and recrystallization might occur, work hardening played a leading role. Because of the slippage of grains in the process of plastic deformation and the tangling of dislocations, the grains were elongated or broken and fibrozed, which resulted in the formation of residual stress in the metal. As the deformation continued to increase, the stress was gradually

reduced due to work softening. The subsequent stress reduction during deformation was mainly due to recovery and recrystallization, and work softening caused by recovery and recrystallization played a leading role in this. The stress gradually approached a stable value and remained constant with an increase in deformation. At this point, the work hardening and work softening of the material were balanced and entered a steady deformation stage [15,16].

The stress and peak stress gradually decreased with an increase in the strain rate under certain temperature conditions. The strain point corresponding to the peak stress increased with the temperature and amount of deformation. The deformation showed the same response at different temperatures; that is, the stress began to rapidly increase due to work hardening and reached a peak as the amount of deformation increased. Then, the stress gradually decreased and stabilized due to the influence of work softening [17,18].

3.2. Construction of Constitutive Equations

The flow stress of the metal during hot deformation is related to the thermodynamic parameter Z and deformation rate $\dot{\varepsilon}$ of the material. The relation is expressed as follows [19,20]:

$$Z = \dot{\varepsilon} exp(\frac{Q}{RT}), \tag{1}$$

where Q is the thermal deformation activation energy of the material, R is the gas constant, and T is the absolute temperature.

Materials have different stress function forms under different conditions, as follows:

$$F(\sigma) = A_1\sigma^n(\alpha\sigma < 0.8) \tag{2}$$

$$F(\sigma) = A_2 exp(\beta\sigma)(\alpha\sigma > 1.2) \tag{3}$$

$$F(\sigma) = A_2 exp(\beta\sigma)(\alpha\sigma > 1.2) \tag{4}$$

where A_i (I = 1, 2, 3); α, β, and n are the material parameters.

The sinusoidal equation proposed by Sellars et al. is generally used to describe the relationship between various material parameters during plastic deformation and is expressed as follows:

$$\dot{\varepsilon} = A[sinh(\alpha\sigma)]^n exp\left[-\frac{Q}{RT}\right] \tag{5}$$

where α, n, A, and β are the material parameters. Q is the thermal deformation activation energy of the material. R is the gas constant, which is a fixed value (R = 8.31). $\dot{\varepsilon}$ is the deformation rate. Σ is the flow stress, and T denotes absolute temperature.

Substituting Equations (2) and (3) into Equation (6) and deriving on two sides of the equation, Equation (7) could be obtained.

$$ln\dot{\varepsilon} = lnA_1 + nln\sigma - \frac{Q}{RT} \tag{6}$$

$$ln\dot{\varepsilon} = lnA_2 + \beta\sigma - \frac{Q}{RT} \tag{7}$$

For convenience, the logarithmic form of the equation is often employed. Then, the corresponding graphs are made with the coordinates of $ln\dot{\varepsilon}$ and $ln\sigma$ and $ln\ \dot{\varepsilon}$ and σ, respectively. As shown in Figure 4, the peak stress corresponding to different strain rates at different temperatures was calculated. The data are also shown in Table 2.

The diagram in Figure 4 could be fitted, where the average slope of each $ln\dot{\varepsilon}$-$ln\sigma_p$ line could be calculated based on Equation (6) and Figure 4a, and the $ln\dot{\varepsilon}$-$ln\sigma_p$ lines could be calculated based on Equation (7) and Figure 4b. The resulting average slopes were n = 5.954252 and β = 0.031217. Given α = β/n, α = 0.0052428 could also be obtained.

Table 2. Strain rate ($\dot{\varepsilon}$), peak stress (σ_p), and corresponding logarithmic value of the GH4169 superalloy at various temperatures.

Temperature T/°C	Strain Rate ($\dot{\varepsilon}$)/s^{-1}	Peak Stress (σ_p)/Mpa	$ln\dot{\varepsilon}$	$ln\sigma_p$	$ln[sinh(\alpha\sigma_p)]$
900	0.001	253.1	−6.908	5.533785	0.5608306
	0.01	364.32	−4.605	5.898033	1.1947405
	0.1	523.39	−2.303	6.260327	2.0467375
	1	556.85	0	6.322296	2.2233897
950	0.001	212.46	−6.908	5.358754	0.3067085
	0.01	354.28	−4.605	5.870088	1.139611
	0.1	450.13	−2.303	6.109536	1.6578382
	1	528.47	0	6.269986	2.0735863
1000	0.001	171.81	−6.908	5.146389	0.0272396
	0.01	347.85	−4.605	5.851771	1.1041569
	0.1	367.16	−2.303	5.905798	1.2102875
	1	500.3	0	6.215208	1.9245429
1050	0.001	82.3	−6.908	4.410371	−0.809689
	0.01	139.68	−4.605	4.939354	−0.22371
	0.1	218.02	−2.303	5.384587	0.3426757
	1	303.52	0	5.715448	0.8557846
1100	0.001	74.45	−6.908	4.310128	−0.915507
	0.01	129.43	−4.605	4.86314	−0.31216
	0.1	178.39	−2.303	5.183972	0.0748297
	1	233.89	0	5.454851	0.443079
1120	0.001	66.847	−6.908	4.202406	−1.028105
	0.01	105.18	−4.605	4.655673	−0.54505
	0.1	158.97	−2.303	5.068716	−0.06898
	1	215.31	0	5.372079	0.3252004

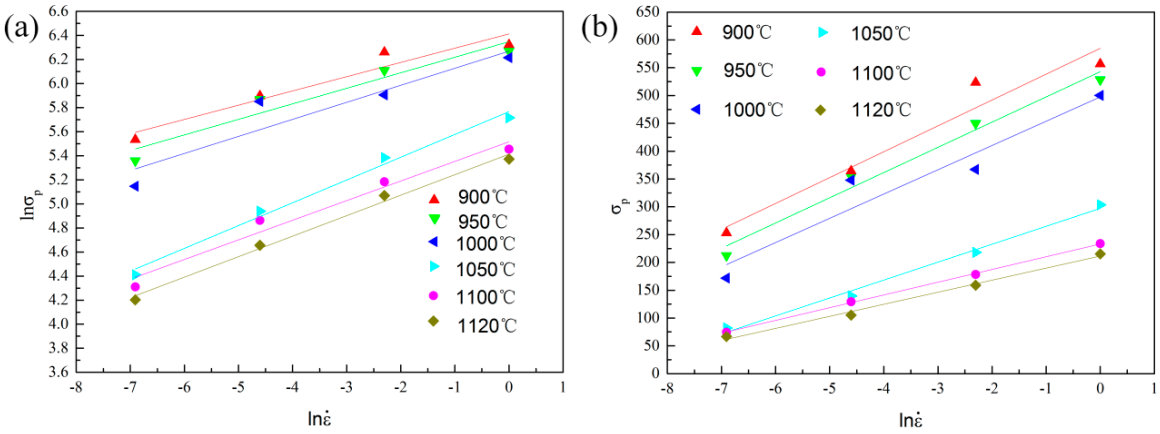

Figure 4. Relation among $ln\sigma_p$, σ_p, and $ln\dot{\varepsilon}$ curves at different temperatures. (**a**) $ln\sigma_p$ and $ln\dot{\varepsilon}$ curves at different temperatures; (**b**) σ_p and $ln\dot{\varepsilon}$ curves at different temperatures.

Deriving on both sides of Formula (6):

$$ln\dot{\varepsilon} = lnA + nln[sinh(\alpha\sigma)] - \frac{Q}{RT} \tag{8}$$

Performing partial derivation of $1/T$ at a certain strain rate for Equation (8) yields:

$$Q = R\left[\frac{\partial ln\dot{\varepsilon}}{\partial ln[sinh(\alpha\sigma)]}\right]_T\left[\frac{\partial ln[sinh(\alpha\sigma)]}{\partial(1/T)}\right] \tag{9}$$

The activation energy of the material is constant when the strain rate is constant. The n values fitted in Figure 4 were substituted into Equation (9) to obtain $ln\dot{\varepsilon}$ and $ln[sinh(\alpha\sigma)]$ at different deformation

temperatures and $ln[sinh(\alpha\sigma)]$ and $1000/T$ at different strain rates, where 1000 times $1/T$ was used for convenient calculation, as shown in Figures 5 and 6.

The average slope k = 0.231755 of each straight line could be calculated based on the straight line fitted in Figure 5, and the average slope of each straight line t = 13.90354 could be calculated based on the straight line fitted in Figure 6. Based on Equation (9), the thermal deformation energy of the material could be calculated as follows:

$$Q = \frac{R * T}{k} = 498.54 \frac{kJ}{mol} = 498540\ J/mol \tag{10}$$

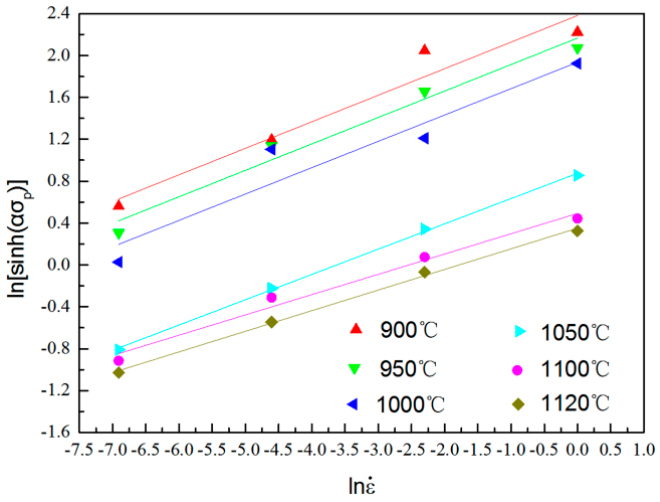

Figure 5. The relation between $ln[sinh(\alpha\sigma_p)]$ and $ln\dot{\varepsilon}$ at various deformation temperatures.

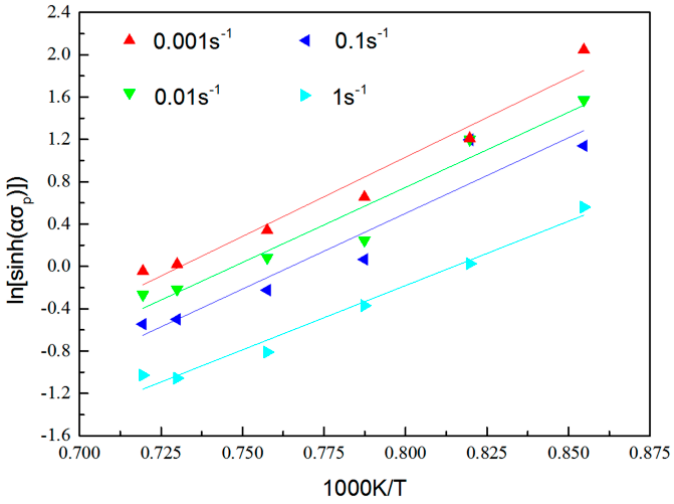

Figure 6. The relation between $ln[\sinh(\alpha\sigma_p)]$ and 1000 K/T at various strain rates.

From Equations (1) and (6), Equation (11) was obtained:

$$Z = \dot{\varepsilon} exp\left(\frac{Q}{RT}\right) = A[sinh(\alpha\sigma)]^n \tag{11}$$

Performing derivation on both sides of Equation (11):

$$lnZ = ln\dot{\varepsilon} + \frac{Q}{RT} \tag{12}$$

$$lnZ = lnA + nln[sinh(\alpha\sigma)] \tag{13}$$

The corresponding value of lnZ could be calculated by comparing the peak stress values for different temperatures and strain rates, and the corresponding lnZ and $ln[sinh(\alpha\sigma_p)]$ maps were fitted using Equation (13), as shown in Figure 7. The slope of the line was n = 4.56568, and the intercept was lnA = 42.21596 ($A = 2.1585 \times 10^{18}$). Thus, $Z = 2.1585 \times 10^{18} \times [sinh(0.0052428\sigma)]^{4.56568}$ was obtained.

Substituting all e values obtained into Equation (6) yielded the constitutive equation of the alloy, as shown in Equation (14).

$$\dot{\varepsilon} = 2.1585 \times 10^{18} \times [sinh(0.0052428\sigma)]^{4.56568} \times exp(-\frac{498540}{RT}) \quad (14)$$

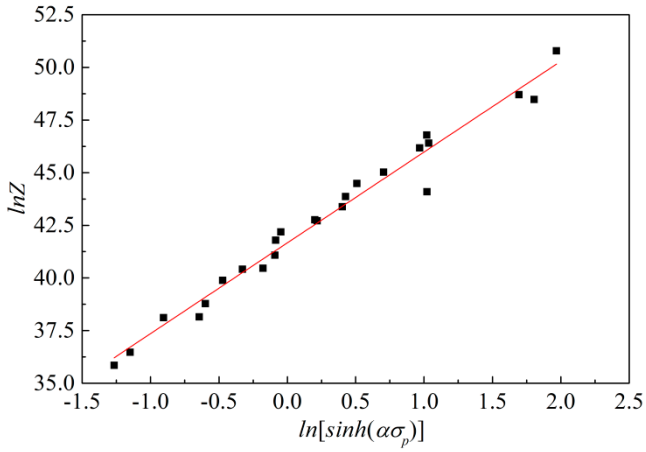

Figure 7. Relation between lnZ and $ln[sinh(\alpha\sigma_p)]$ at various strain rates and deformation temperatures.

3.3. Dynamic Recrystallization Model

3.3.1. Proposed Model

Existing studies generally use the Avrami equation to describe the recrystallization degree quantitatively [21,22]:

$$X = 1 - exp[-k(\frac{\varepsilon - \varepsilon_c}{\varepsilon_{0.5}})^n] \quad (15)$$

where X is the dynamically recrystallized volume fraction of the material; k and n are the material parameters; ε is a dependent variable; ε_c is the critical strain; $\varepsilon_{0.5}$ is the recrystallized amount of the material when 50% strain is reached.

Peak strain model:

$$\varepsilon_p = AZ^m \quad (16)$$

where A and m are the material parameters; Z is the temperature compensation factor.

Critical strain model:

$$\varepsilon_c = k\varepsilon_p \quad (17)$$

where k ranges from 0.6 to 0.85, and a value of 0.8 was used in this study.

A quantitative description of the recrystallization quality is usually given by:

$$D_{2-drex} = A_1 Z^{A_2} \quad (18)$$

where A_1 and A_2 are material-dependent constants.

3.3.2. Model Establishment

The peak strain value of the material during hot deformation could be obtained through experiments, and the corresponding recrystallization volume fraction and lnZ value were calculated, as shown in Table 3.

Simplifying Equation (16) yielded:

$$ln\varepsilon_p = lnA + mlnZ \tag{19}$$

As shown in Equation (18), the corresponding $ln\varepsilon_p$ and lnZ maps could be constructed and fitted (Figure 8). The intercept of the line was $lnA = -4.46775$, that is, $A = 1.15 \times 10^{-2}$, and the slope of the line was $m = 0.067$.

Substituting the obtained A and m values into Equation (16) yielded Equation (20).

$$\varepsilon_p = 1.15 \times 10^{-2} Z^{0.067} \tag{20}$$

Then, by Equation (17):

$$\varepsilon_c = 9.2 \times 10^{-3} Z^{0.067} \tag{21}$$

The strain value corresponding to material recrystallization of 50% could be obtained by performing Newton interpolation on the parameter values obtained from the experiment, as shown in Equation (22).

$$\varepsilon_{0.5} = 0.29 Z^{0.016} \tag{22}$$

Simplifying Equation (15) yielded:

$$ln\left[ln\left(\frac{1}{1-X}\right)\right] = lnk + nln\left(\frac{\varepsilon - \varepsilon_c}{\varepsilon_{0.5}}\right) \tag{23}$$

The corresponding $ln\{ln[1/(1 - X)]\}$ and $ln[(\varepsilon - \varepsilon_c)/\varepsilon_{0.5}]$ maps could be constructed from Equation (23), and a linear fit could be performed, as shown in Figure 9. By fitting the data in Figure 9, one found $k = 0.812$ and $n = 0.92$.

Substituting the values of k and n into Equation (15) yielded:

$$X = 1 - exp\left[-0.812\left(\frac{\varepsilon - \varepsilon_c}{\varepsilon_{0.5}}\right)^{0.92}\right] \tag{24}$$

Table 3. Strain rate $\dot{\varepsilon}$, peak strain ε_p, dynamic recrystallization volume fraction X, and lnZ at different temperatures.

Temperature/°C	Srain Rate $\dot{\varepsilon}$/s^{-1}	Peak Strain ε_p/MPa	lnZ	X
950	0.001	0.221	42.26602	0.724
	0.01	0.156	40.33004	0.658
	0.1	0.105	38.54073	0.543
	1	0.113	36.88203	0.287
1000	0.001	0.1	36.25196	0.927
	0.01	0.228	44.5686	0.843
	0.1	0.2	42.63263	0.706
	1	0.168	40.84331	0.504
1050	0.001	0.154	39.18461	0.895
	0.01	0.144	38.55454	0.919
	0.1	0.232	46.87119	0.817
	1	0.221	44.93521	0.665
1100	0.001	0.206	43.1459	0.905
	0.01	0.188	41.4872	0.928
	0.1	0.18	40.85713	0.886
	1	0.237	49.17377	0.780
1120	0.001	0.233	47.2378	0.887
	0.01	0.225	45.44848	0.928
	0.1	0.212	43.78978	0.904
	1	0.206	43.15971	0.815

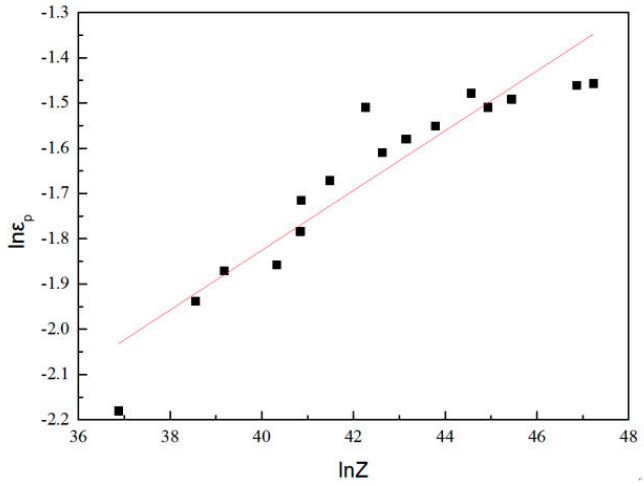

Figure 8. The relation between lnZ and $ln\varepsilon_p$ at various deformation temperatures.

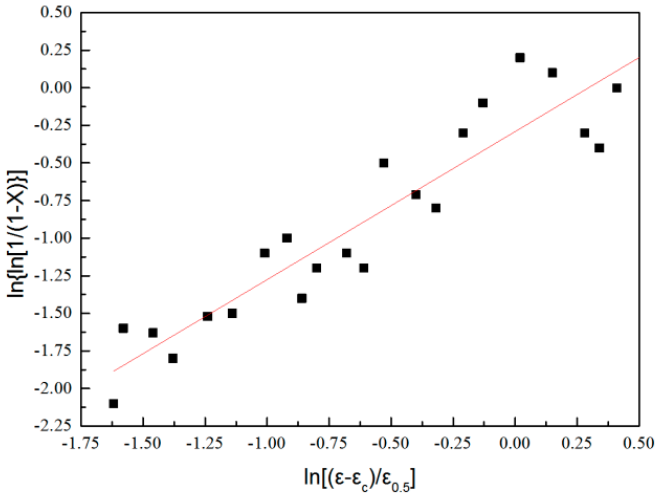

Figure 9. Relation between $ln\{ln[1/(1-X)]\}$ and $ln[(\varepsilon-\varepsilon_c)/\varepsilon_{0.5}]$ at various deformation temperatures.

The grain size of the microstructure calculated according to the GH4169 high-temperature dynamic recrystallization metallographic structure diagram is shown in Table 4. According to the data in the table, the logarithmic fitting of $D_{2\text{-}drex}$ and Z could be used to find the corresponding model parameters. The fitted image is shown in Figure 10. The obtained dynamic recrystallization crystal mass equation is shown in Equation (25).

$$D_{2-drex} = 3\times10^{6}Z^{-0.3016} \quad (25)$$

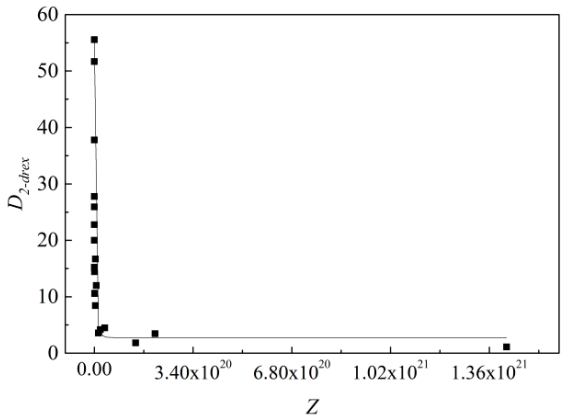

Figure 10. $D_{2\text{-}drex}$ and Z fitted image.

Table 4. Strain rate $\dot{\varepsilon}$, dynamic recrystallization grain size, and Z of the GH4169 superalloy at various temperatures.

Temperature/°C	Strain Rate/s^{-1}	Z	$D_{2\text{-}drex}$/μm
950	0.001	1.42×10^{18}	10.556
	0.01	1.42×10^{19}	3.578
	0.1	1.42×10^{20}	1.818
	1	1.42×10^{21}	1.111
1000	0.001	2.09×10^{17}	22.78
	0.01	2.09×10^{18}	10.603
	0.1	2.09×10^{19}	4.167
	1	2.09×10^{20}	3.442
1050	0.001	3.57×10^{16}	37.78
	0.01	3.57×10^{17}	15.2
	0.1	3.57×10^{18}	8.425
	1	3.57×10^{19}	4.487
1100	0.001	6.93×10^{15}	51.67
	0.01	6.93×10^{16}	25.92
	0.1	6.93×10^{17}	14.444
	1	6.93×10^{18}	12
1120	0.001	3.72×10^{15}	55.56
	0.01	3.72×10^{16}	27.78
	0.1	3.72×10^{17}	20
	1	3.72×10^{18}	16.667

3.4. Double-Open Multidirectional Forging Simulation

3.4.1. Process and Finite Element Model

The finite element model used in the simulation is shown in Figure 11. During forging, the initial billet was compressed in the height direction, stretched in the longitudinal direction, and did not deform in the width direction, owing to the restraining effect of the mold. When the amount of deformation reached a certain level, the closed multidirectional forging occurred due to the restraining action of the lower die, the length of the forging was no longer increased in the longitudinal direction, and the groove of the lower die was gradually filled. Meanwhile, the single-open multidirectional forging side was full, the other side maintained a free surface, and the sides of the double-open multidirectional forging maintained a free surface. The forging was rotated by 90° every time it was swept, and the last forging was repeated. The simulation utilized a relative net partitioning method and a tetrahedral mesh with 20,000 cells. Table 5 shows the parameter settings used for the double-open multidirectional forging simulation.

Table 5. Parameter list.

Process Parameters	Symbol	Unit	Value
Forging size	-	mm	40 × 40 × 50
Mold material	-	-	H13
Forging temperature	T	°C	800–1000
Coefficient of friction	f	-	0.3
Thermal conductivity	λ	W/(m·K)	20–40
Specific heat	C	N/(mm^2·K)	3–5
Initial grain size	d	μm	45
Upper die size	-	mm	50 × 40 × 10
Lower die size	-	mm	70 × 60 × 60
Reduction rate	-	%	20

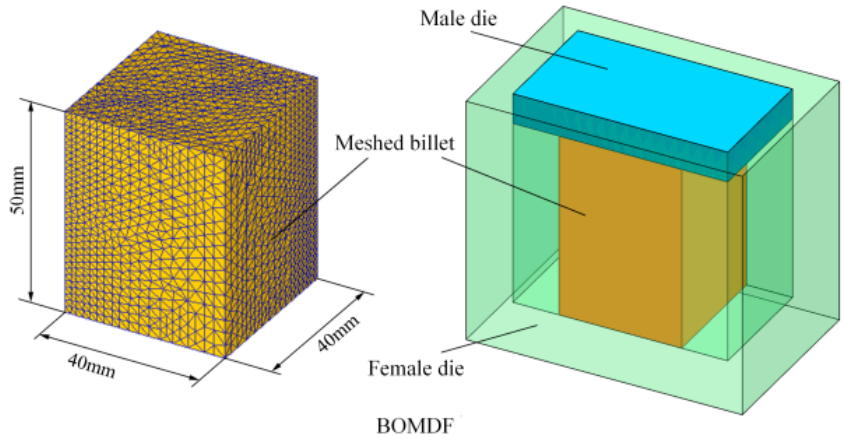

Figure 11. Finite element model.

3.4.2. Numerical Simulation Results and Analysis

Figure 12 shows the dynamic recrystallization volume fraction cloud diagram of forgings from three to nine passes at 800 °C. The dynamic recrystallization volume fraction of the forging was symmetrically distributed and could be divided into three deformation zones, namely difficult, easy, and free. The equivalent strain was minimized on the outer surface of the forging due to the restraint of the mold. Therefore, the recrystallization degree in this area was relatively low, the area with the largest recrystallization was approximately 30%, and some areas were not recrystallized. In the interior of the forging, the equivalent strain was large, and the recrystallization degree was relatively high because it was not affected by the mold friction. The recrystallization degree near the inner forging was high, and the center portion reached approximately 82%.

Figure 13 shows the recrystallized grain size graph of forging from three to nine passes at 800 °C. The cloud diagram shows that the recrystallized grain size of the forging was symmetrically distributed. The closer it was to the forging center, the smaller was the grain size. The equivalent strain of the forging was also small on the outer surface of the forging due to the limitation of the die on the forging, thereby affecting the recrystallization. Thus, the average grain size of the forging in this area was large, and no recrystallization occurred. The equivalent strain in the interior of the forging was large because it was not affected by the mold friction. Thus, the average grain size was small, with a minimum value of approximately 33.5 μm.

The recrystallization degree of the forgings was remarkably improved when it reached six passes. The closer it was to the internal, the higher was the recrystallization degree, which resulted in the center portion to approximately reach 95.5%. Therefore, the recrystallization degree was high, and the average grain size was small. The minimum value was approximately 12.2 μm. When forging nine passes, the recrystallization degree of the forgings reached 98.5%, and the minimum average grain size was approximately 5.1 μm.

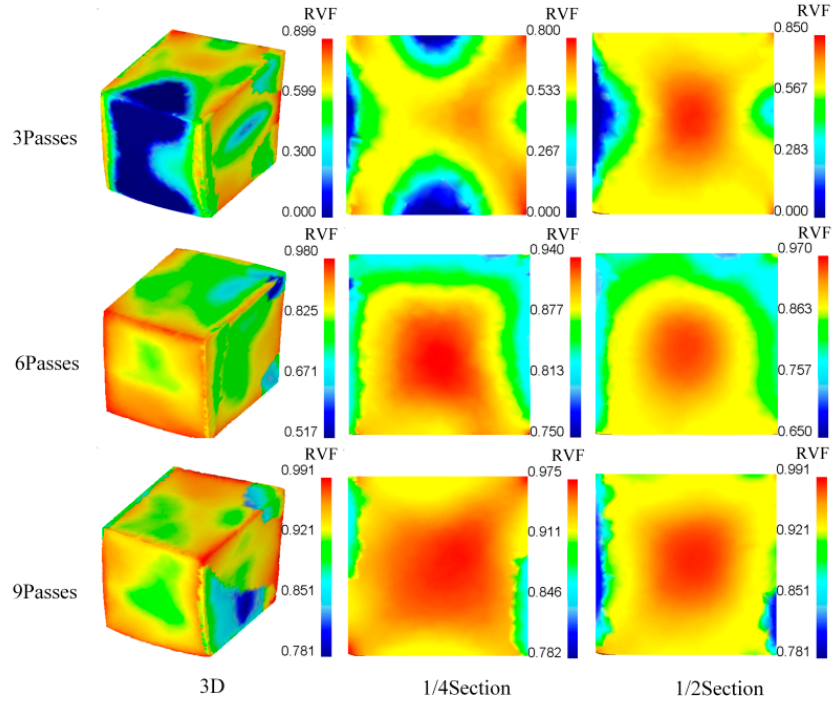

Figure 12. Dynamic recrystallization volume fraction cloud diagram for three to nine passes forging at 800 °C.

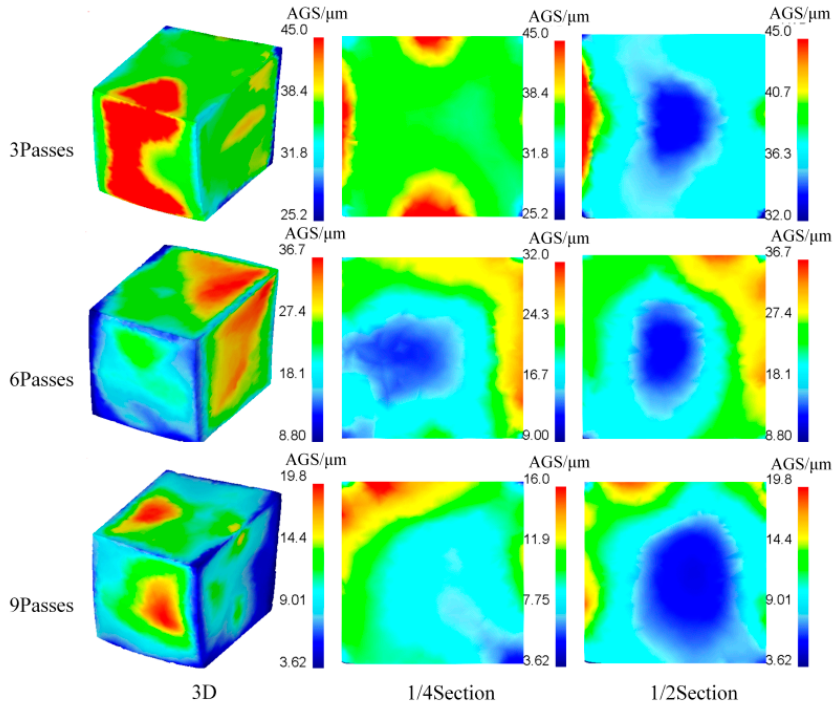

Figure 13. Forging of three to nine passes for recrystallized grain size cloud map at 800 °C.

Figure 14 shows the dynamic recrystallization volume fraction cloud diagram of forging from three to nine passes at 900 °C. From the figure, the dynamic recrystallization volume fraction of the forging was symmetrically distributed and could be divided into three deformation zones: difficult, easy, and free deformation. The equivalent strain was minimized on the outer surface due to the mold constraint. Therefore, the recrystallization degree in this area was relatively low, the area with the largest recrystallization was approximately 50%, and some areas were not recrystallized. In the interior of the forging, because it was not affected by the mold friction, the equivalent strain was large;

the recrystallization degree was relatively high, and the closer it was to the internal, the higher was the recrystallization degree, which resulted in the center portion achieving a value of approximately 87%.

Figure 15 shows the recrystallized grain size cloud diagram of forging from three to nine passes at 900 °C. From the figure, the recrystallized grain size of the forging was symmetrically distributed, and the closer it was to the inside of the forging, the smaller was the grain size, and the closer the outer grain size was, the larger was the grain size. The equivalent strain was small on the outer surface of the forging due to the limitation of the die on the forging, which affected its recrystallization. Thus, the average grain size of the forging in this area was large, and no recrystallization occurred. In the interior of the forging, because it was not affected by the mold friction, the equivalent strain was large. Thus, the recrystallization degree in this region was high, the average grain size was small, and the minimum value was approximately 26 μm.

The center portion reached approximately 97.5% under the forging of six passes. Therefore, the recrystallization degree was high in this region, the average grain size was small, and the minimum value was approximately 10 μm. When forging nine passes, the recrystallization degree of the forgings reached approximately 99.7%, and the average grain size minimum was approximately 4 μm.

Figure 16 shows the dynamic recrystallization volume fraction cloud diagram of forgings from three to nine passes at 1000 °C. From the figure, the dynamic recrystallization volume fraction of the forging was symmetrically distributed and could be divided into three deformation zones: difficult, easy, and free deformation zones. The equivalent strain was minimized on the outer surface of the forging due to the constraint of the mold. Thus, the recrystallization degree in this area was relatively low, and the area with the largest recrystallization was approximately 70%. In the interior of the forging, because it was not affected by the mold friction, the equivalent strain was large, and the recrystallization degree was relatively high. The closer it was to the internal, the higher was the recrystallization degree, which resulted in the highest value of approximately 74% at the center; moreover, the degree of internal recrystallization did not change considerably with the outside. No obvious increasing trend was observed.

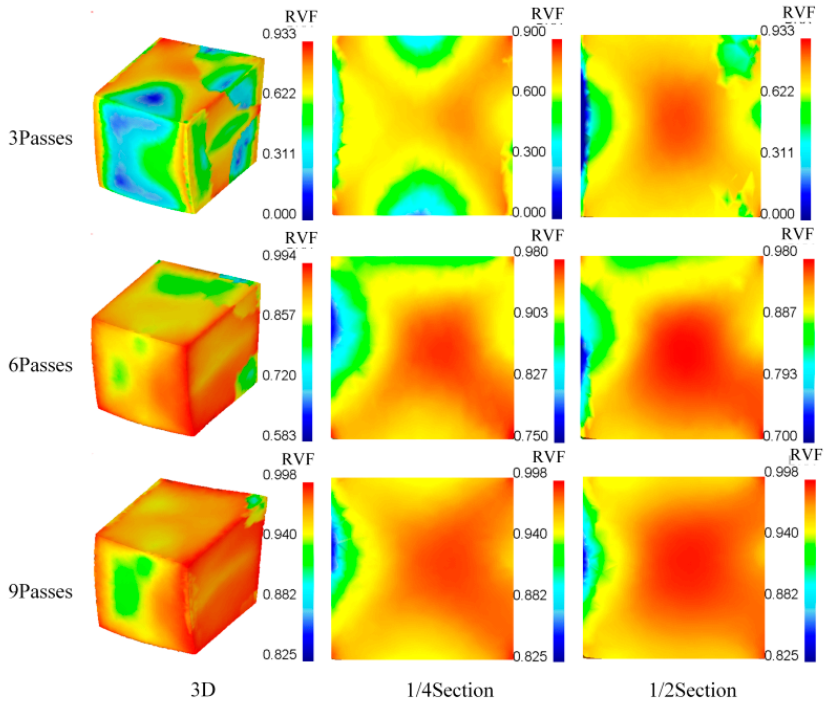

Figure 14. Forging from three to nine passes for dynamic recrystallization volume fraction cloud image at 900 °C.

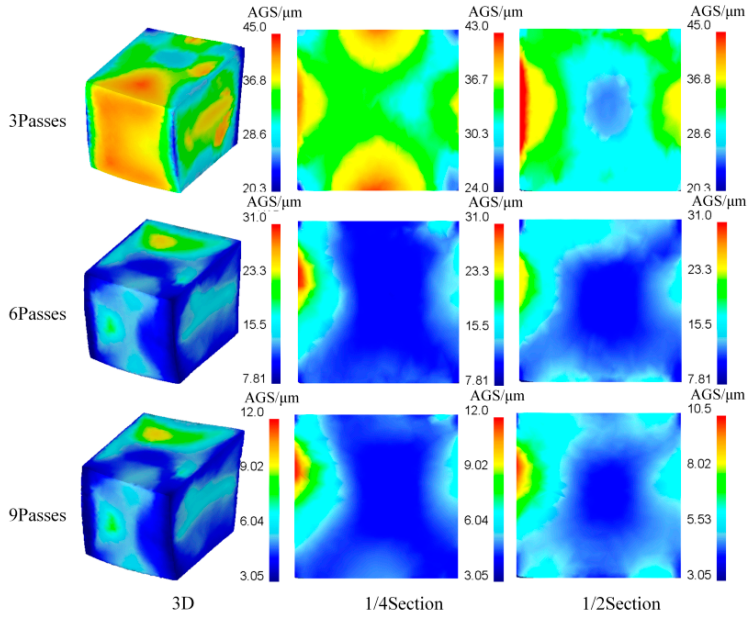

Figure 15. Forging from three to nine passes for recrystallized grain size cloud image at 900 °C.

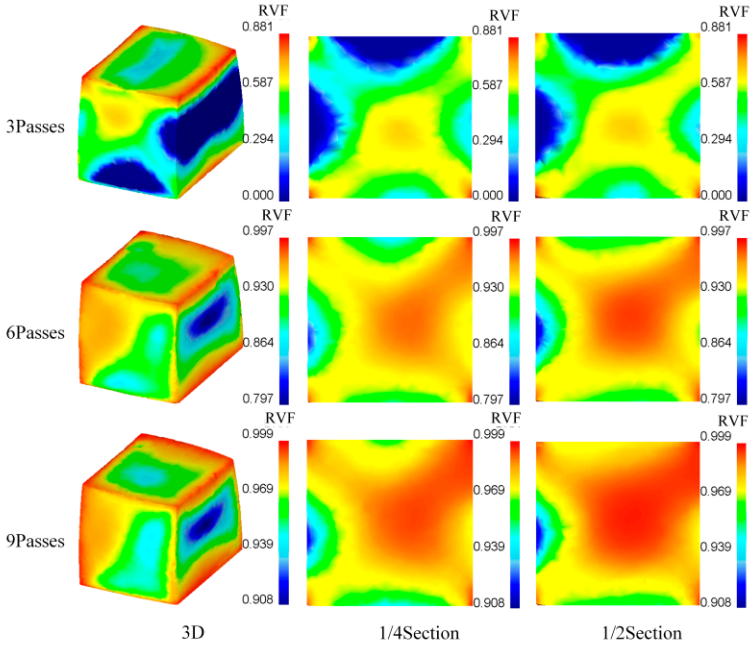

Figure 16. Dynamic recrystallization volume fraction cloud image of forging from three to nine passes at 1000 °C.

Figure 17 shows the recrystallized grain size graph of forging from three to nine passes at 1000 °C. From the figure, the recrystallized grain size of the forging was symmetrically distributed; moreover, the closer it was to the inside of the forging, the smaller was the grain size, and the closer it was to the outer grain size, the larger was the grain size. The equivalent strain was small on the outer surface of the forging due to the restraining effect of the die on the forging, which affected the recrystallization of the forging. The average grain size of the forging in this area was relatively large. In the interior of the forging, because it was not affected by the mold friction, the equivalent strain was large. Thus, the recrystallization degree in this area was relatively high, the average grain size was small, the minimum value was approximately 24 μm, and the internal and external grain sizes of the forging did not change significantly. This situation occurred because the deformation temperature of the forging was relatively high, and the strain had no considerable effect on recrystallization.

The center portion approximately reached 99% with the forging of six passes. Therefore, the recrystallization degree was high in this region, the average grain size was small, and the minimum value was approximately 9.1 μm. When forging nine passes, all areas of recrystallization volume fraction exceeded 95%, the grain size was 3–5.5 μm, the recrystallization degree of forgings reached 99.7%, and the average grain size minimum was approximately 3 μm.

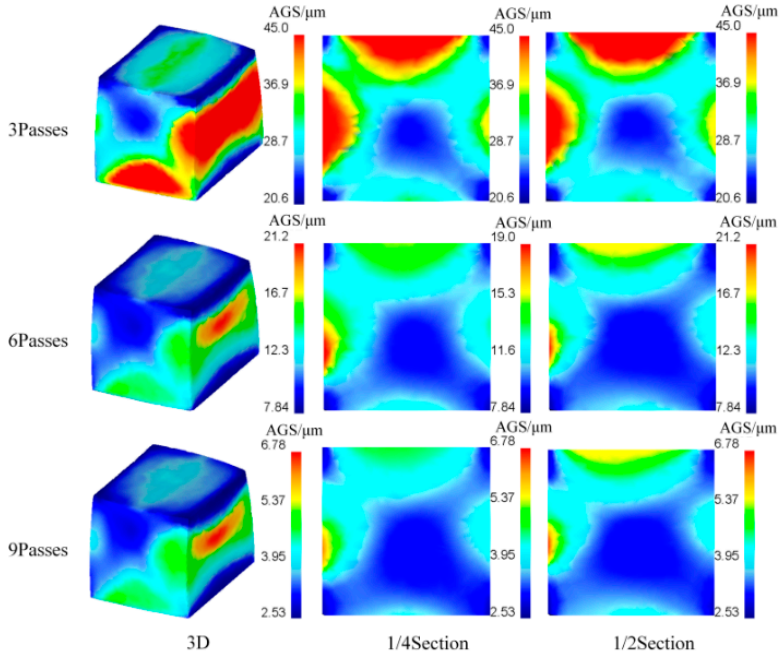

Figure 17. Recrystallization grain size cloud image of forging from three to nine passes at 1000 °C.

4. Conclusions

(1) Based on the thermal compression experiment, the constitutive model of the material and the mathematical model of recrystallization evolution were derived by analyzing the stress-strain curve of GH4169 and applied to the secondary development of software. A simulation of the microstructure evolution law in the double-open multi-directional forging process was conducted.

(2) The evolution rule of the recrystallization volume fraction and the recrystallized grain size of the GH4169 superalloy double-open multidirectional forging was obtained. Increasing the forging temperature increased the recrystallization volume fraction and reduced the recrystallization grain size. Performing more passes had the same effect and led to more complete recrystallization and a smaller recrystallized grain size. At 1000 °C and nine passes, the recrystallization volume fraction exceeded 95%, and the recrystallized grain size reached the minimum size of 3–5.5 μm.

Author Contributions: J.L. and Y.J. conceived and designed the experiments; H.X., S.W., and Z.Y. performed the experiments; L.Z. and C.Z. analyzed the data; J.L. and Y.J. wrote the paper.

Funding: This project is supported by Natural Science Foundation of Hebei Province, China (Grant No. E2019203005).

Conflicts of Interest: The authors declare no conflict of interest.

References

1. Zhou, L.X.; Baker, T.N. Eeffct of strain rate and temperuatre on deofrmation behvaior of IN718 during high temperuatre deformation. *Mater. Sci. Eng.* **1994**, *177*, 1–9. [CrossRef]
2. Du, J.H.; Lu, X.D.; Deng, Q.; Bi, Z.B. Progress in the Research and Manufacture of GH4169 alloy. *J. Iron Steel Res. Int.* **2015**, *22*, 657–663. [CrossRef]

3. Li, H.Y.; Kong, Y.H.; Chen, G.S.; Xie, L.X.; Zhu, S.G.; Sheng, X. Effect of different processing technologies and heat treatments on the microstructure and creep behavior of GH4169 superalloy. *Mater. Sci. Eng.* **2013**, *582*, 368–373. [CrossRef]
4. Zhou, X.; Zhang, J.; Chen, X.; Zhang, X.; Li, M. Fabrication of high-strength AZ80 alloys via multidirectional forging in air with no need of ageing treatment. *J. Alloys Compd.* **2019**, *787*, 551–559. [CrossRef]
5. Na, Y.S.; Yeom, J.T.; Park, N.K.; Lee, J.Y. Simulation of microstructures for Alloy 718 blade forging using 3D FEM simulator. *J. Mater. Process. Technol.* **2003**, *141*, 337–342. [CrossRef]
6. Salevati, M.A.; Akbaripanah, F.; Mahmudi, R. Microstructure, Texture, and Mechanical Properties of AM60 Magnesium Alloy Processed by Extrusion and Multidirectional Forging. *J. Mater. Eng. Perform.* **2019**, *28*, 3021–3030. [CrossRef]
7. Miura, H.; Maruoka, T.; Yang, X.; Jonas, J.J. Microstructure and mechanical properties of multi-directionally forged Mg–Al–Zn alloy. *Scr. Mater.* **2012**, *66*, 49–51. [CrossRef]
8. Kishchik, M.S.; Mikhaylovskaya, A.V.; Kotov, A.D.; Mosleh, A.O.; AbuShanab, W.S.; Portnoy, V.K. Effect of multidirectional forging on the grain structure and mechanical properties of the Al–Mg–Mn alloy. *Materials* **2018**, *11*, 2166. [CrossRef]
9. Xia, X.S.; Wang, C.P.; Wu, Y.; Zhang, K.; Ma, M.L.; Yuan, B.G. Grain refinement, microstructure and mechanical properties homogeneity of Mg-Gd-Y-Nd-Zr alloy during multidirectional forging. *J. Mater. Eng. Perform.* **2018**, *27*, 5689–5699. [CrossRef]
10. Aoba, T.; Kobayashi, M.; Miura, H. Microstructural evolution and enhanced mechanical properties by multi-directional forging and aging of 6000 series aluminum alloy. *Mater. Trans.* **2018**, *59*, 373–379. [CrossRef]
11. Lin, J.; Liu, Y. A set of unified constitutive equations for modellling microstructure evolution in hot deformation. *J. Mater. Process. Technol.* **2003**, *143*, 281–285. [CrossRef]
12. Kermanpur, A.; Lee, P.D.; Mclean, M.; Tin, S. Integrated modeling for the manufacture of aerospace discs: Grain structure evolution. *JOM* **2004**, *56*, 72–78. [CrossRef]
13. Tin, S.; Lee, P.D.; Kermanpur, A.; Mclean, M.; Rist, M. Integrated modeling for the manufacture of Ni-based superalloy discs from solidification to final heat treatment. *Metall. Mater. Trans. A* **2005**, *36*, 2493–2504. [CrossRef]
14. Park, N.K.; Kim, I.S.; Na, Y.S.; Yeom, J.T. Hot forging of a nickel-base superalloy. *J. Mater. Process. Technol.* **2001**, *111*, 98–102. [CrossRef]
15. Murty, S.V.S.N.; Rao, B.N. On the development of instability criteria during hotworking with reference to IN 718. *Mater. Sci. Eng.* **1998**, *254*, 76–82. [CrossRef]
16. Cao, F.R.; Zhang, J.; Ding, X.; Xue, G.Q.; Liu, S.Y.; Sun, C.F. Mechanical properties and microstructural evolution in a superlight Mg-6.4Li-3.6Zn-0.37Al-0.36Y alloy processed by multidirectional forging and rolling. *Mater. Sci. Eng.* **2019**, *760*, 377–393. [CrossRef]
17. Marty, B.; Guedou, J.; Gergaud, P.; Lebrun, J.L. Recrystallization and work-hardening prediction during forging process of inconel 718. *Superalloys* **1997**, *718*, 625–706.
18. Zhang, Z.X.; Qu, S.J.; Feng, A.H.; Hu, X.; Shen, J. Microstructural mechanisms during multidirectional isothermal forging of as-cast Ti-6Al-4V alloy with an initial lamellar microstructure. *J. Alloys Compd.* **2019**, *773*, 277–287. [CrossRef]
19. Zhang, J.M.; Gao, Z.Y.; Zhuang, J.Y.; Zhong, Z.Y. Mathematical modeling of the hot deformation behavior of superally IN718. *Metall. Mater. Trans. A* **1999**, *30*, 2701–2713. [CrossRef]
20. Thomas, A.; El-Wahabi, M.; Cabrera, J.M.; Prado, J.M. High temperature deformation of Inconel 718. *J. Mater. Process. Technol.* **2006**, *177*, 469–472. [CrossRef]
21. Hu, J.P.; Zhuang, J.Y.; Du, J.H.; Deng, Q.; Feng, D. Constitutive equation of superalloy In718 in hammer forging process. *J. Iron Steel Res. Int.* **2001**, *8*, 50–54.
22. Dandre, C.A.; Roberts, S.M.; Evans, R.W.; Reed, R.C. Microstructural evolution of Inconel* 718 during ingot breakdown: Process modelling and validation. *Mater. Sci. Technol.* **2000**, *16*, 14–25. [CrossRef]